ISSN: 1411-5719(p): 2655-500X (e),
Volume 23 Nomor 1 (June 2026): 1–20

Soil and Water Journal
Jurnal Tanah dan Air

RESEARCH ARTICLE OPEN ACCESS

GEOCHEMISTRY, WEATHERING CHARACTERISTICS, AND MINERALOGY OF THE RESIDUAL SOILS DEVELOPED FROM NOTOPURO TUFF, CENTRAL JAVA, INDONESIA

Hakim Erlangga Bernado Sakti[1*)], Sari Bahagiarti Kusumayudha[1)], Mohammad Nurcholis[2)], Joko Soesilo[1)], and Nazario Gomes[3)]

[1)] Geological Engineering Department, Universitas Pembangunan Nasional "Veteran" Yogyakarta, Sleman, Indonesia, 55283
[2)] Soil Science Department, Universitas Pembangunan Nasional "Veteran" Yogyakarta, Sleman, Indonesia, 55283
[3)] Petroleum Engineering, Dili Institute of Technology, Timor Leste

*) Corresponding author: hakimerlangga@upnyk.ac.id

ABSTRACT

Article history:
Received: 2026-01-26
Revised: 2026-06-02
Accepted: 2026-07-29
Published: 2026-08-15
DOI : 10.31315/jta.v23i1.16438

The Notopuro Formation tuff in the border of Sragen and Boyolali Regencies, Central Java, is a region with strategic economic importance and agricultural productivity. Nevertheless, this region has been subject to limited geochemical, weathering, and mineralogical research. Understanding these characteristics is vital for safe construction and land use, which can be a leading indicator that influences agricultural potential and geotechnical challenges. This study aims to fill this knowledge gap by comprehensively analyzing the geochemistry, weathering, and mineralogy of the Notopuro Tuff and its residual soils. Advanced techniques such as scanning electron microscopy (SEM), thin section petrography, and X-ray diffraction (XRD) will be employed. Observed weathering involves Al_2O_3 and Fe_2O_3 enrichment. SiO_2 stability suggests kaolinitization, not lateritization or bauxitization. The tuff originates from a basaltic andesite magma with low-K, calcic, and magnesian affinity, exhibiting metaluminous alumina saturation. Its composition is primarily lithic fragments (50%) and volcanic glass (39%). Weathered tuff crystal minerals include microcline and quartz, with notable cristobalite and magnetite, and generally low crystallinity.

Keywords: Chemical composition, chemical weathering index, degree of crystallinity, mineral semi quantification, weathering stages

How to cite:
Sakti, H.E.B., Kusumayudha, S.B., Nurcholis, M., Soesilo, J & Gomes, N. 2026. Geochemistry, weathering characteristics, and mineralogy of residual soils developed from Notopuro Tuff, Central Java, Indonesia. *Soil and Water Journal.* 23 (01): 1–20. DOI: 10.31315/jta.v23i1.16438

INTRODUCTION

The Notopuro Tuff formation, located in the western region of Sragen, Central Java, is a significant geological feature with extensive distribution. This area serves as a strategic economic corridor connecting the Greater Solo and Kedungsepur (Greater Semarang) Metropolitan Area, which is expected to undergo massive infrastructure development. Despite its strategic importance, detailed studies on the mineralogical and geochemical properties of the Notopuro Tuff and its residual soils are limited. Understanding these properties is crucial for assessing the potential risks associated with construction and land use in this rapidly developing region (Sragen Regency Government, 2011).

Weathered tuff soils are characterized by distinct mineral compositions, particularly enriched in secondary clay minerals produced through authigenic processes. The predominant clay types include smectite (e.g., montmorillonite, nontronite), kaolinite, halloysite, illite, and mixed-layer clays like illite-smectite and kaolinite-smectite. Zeolite minerals frequently arise from interactions between volcanic glass and alkaline water, contributing crucial secondary components to zeolitized tuff. The impact of chemical and mineralogical composition on soil properties, such as cation exchange capacity, plasticity, water retention, and nutrient dynamics, underscores the agricultural potential and geotechnical challenges of weathered tuff soils in stability contexts (Bhavya & Nagaraj, 2025; Indrawan et al., 2024; Korkanç & Solak, 2016; Zhou et al., 2019).

Despite the foundational work in understanding the broader geological context of Central Java, there remains a significant gap in the detailed geochemical and mineralogical characterization of the Notopuro Tuff and its residual soil. Existing studies have not fully explored the implications of mineralogy, geochemistry, weathering stages, stability, and construction suitability in this economically strategic region. This gap highlights the need for focused research to bridge the disconnect between theoretical expectations and practical applications in geotechnical engineering.

To address this gap, the proposed research will focus on comprehensive geochemical, weathering characteristics, and mineralogy of the Notopuro Tuff and its residual soils. Advanced analytical techniques i.e., scanning electron microscopy (SEM), thin section petrography, and X-ray diffraction (XRD), will be employed to assess mineralogy and geochemical characteristics. This approach aims to provide a detailed understanding of the material properties that influence soil behavior and construction suitability, thereby informing infrastructure development strategies in the region.

The urgency of this research lies in its potential to inform sustainable development practices in a rapidly urbanizing area. By elucidating the geochemical, weathering characteristics, and mineralogy of the Notopuro Tuff, this study will contribute to the theoretical understanding of soil behavior and provide practical insights for infrastructure planning and risk management in Central Java. The findings will be crucial for policymakers, engineers, and geologists involved in regional development projects.

MATERIALS AND METHODS

The research was carried out in the border area between Sragen and Boyolali Regencies, Central Java, Indonesia (see Figure 1). The 2 soil profiles examined are a cliff section that has resulted from soil mining activities. Profile 1 is located in Sragen

Regency, while Profile 2 is located in Boyolali Regency. The initial profile measures 100 cm in depth. Profile 2 has a depth of 180 cm. The purpose of observing the soil profiles is to determine the diversity of soil constituents and the evolution of the soil that has taken place. The entire research sample underwent Scanning Electron Microscopy-Energy Dispersive X-ray Spectroscopy (SEM-EDS) with elemental mapping for geochemical analysis. For mineralogical analysis, soil samples were sent to the laboratory, i.e., X-Ray Diffraction (XRD), and tuff sampling was conducted in the laboratory using thin section petrography. The detailed explanation of the laboratory tests along with the analysis is provided in the following paragraphs.

The first and second research objectives, namely geochemical characterization and weathering, were analyzed using Scanning Electron Microscopy with Energy Dispersive X-ray Spectroscopy (SEM EDS) testing. The analytical stages of SEM EDS involve a systematic approach to element mapping for understanding the spatial distribution of elements within the samples. Initially, samples are prepared and mounted to ensure optimal electron beam interaction. The material used for coating the samples is platinum. The next step involved the acquisition of high-resolution images that reveal the morphological characteristics of minerals. This morphology was used to identify mineral types and understand their textural relationships. The type of mineral was determined based on morphological similarity to the mineral obtained from previous studies related to mineral morphology under SEM observation. Subsequently, SEM EDS is employed to perform semi-quantitative compositional analysis, providing insights into the elemental composition and the chemical state of the minerals. The data obtained are then processed to generate elemental maps, which visually represent the distribution of the chemical elements and their oxides across the sample surface. The results from the chemical elemental analysis of the soil and rock samples were subsequently employed to determine the stages of the weathering process using the Chemical Index of Alteration (CIA) method (Nesbitt & Young, 1982), the Mafic Index of Alteration (MIA), and the Index of Lateritization (IOL)/Index of Bauxitization (IOB) (Babechuk et al., 2014) and ternary diagrams for weathering, lateritization, and bauxitization processes (Babechuk & Fedo, 2023). The formulas for CIA, MIA, and IOL can be found in Equations 1 to 4.

$$CIA = \left(\frac{Al_2O_3}{Al_2O_3 + CaO^* + Na_2O + K_2O}\right) \times 100 \quad (1)$$

$$MIA(O) = \left(\frac{Al_2O_3 + Fe_2O_3(T)}{Al_2O_3 + Fe_2O_3(T) + MgO + CaO^* + Na_2O + K_2O}\right) \times 100 \quad (2)$$

$$MIA(R) = \left(\frac{Al_2O_3}{Al_2O_3 + FeO + MgO + CaO^* + Na_2O + K_2O}\right) \times 100 \quad (3)$$

$$IOL/IOB = \left(\frac{Al_2O_3 + Fe_2O_3(T)}{SiO_2 + Al_2O_3 + Fe_2O_3(T)}\right) \times 100 \quad (4)$$

The CIA and MIA use the anhydrous molar ratio, while the IOL/IOB uses the anhydrous mass percentage (%wt). The CaO* value represents the molar ratio of CaO originating solely from silicate minerals, excluding that from carbonate and apatite minerals. It should be emphasized that IOL and IOB fundamentally share one formula. The term IOL is used when there is a tendency for Fe_2O_3 enrichment, whereas the term IOB is used when the tendency observed is Al_2O_3 enrichment (Babechuk et al., 2014; Babechuk & Fedo, 2023; Nesbitt & Young, 1982). The third research objective is the analysis of mineralogical characteristics, which was conducted using XRD testing and thin section petrography. Explanations of these two tests are discussed in the following two paragraphs.

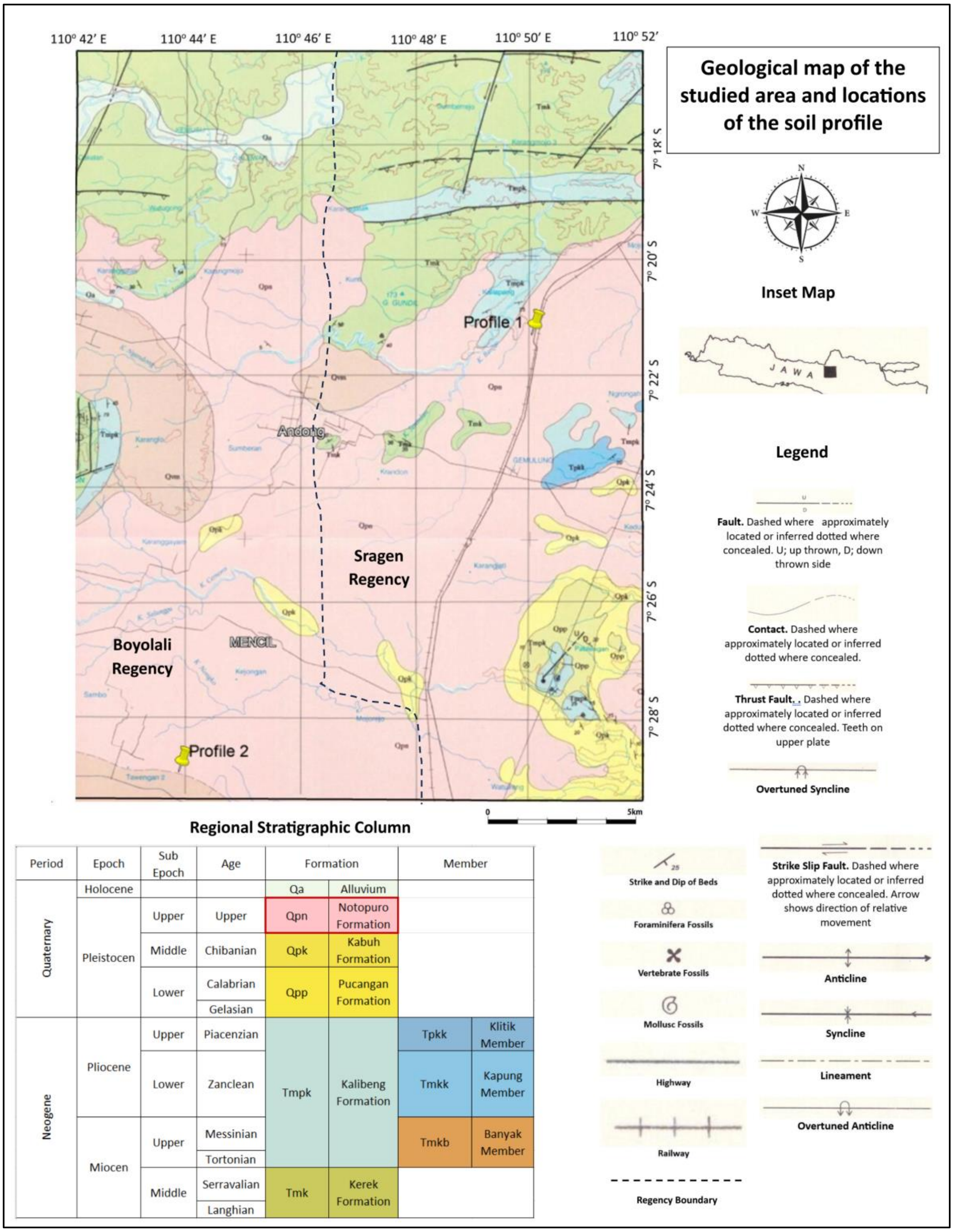

Period	Epoch	Sub Epoch	Age	Formation		Member	
Quaternary	Holocene			Qa	Alluvium		
	Pleistocen	Upper	Upper	Qpn	Notopuro Formation		
		Middle	Chibanian	Qpk	Kabuh Formation		
		Lower	Calabrian	Qpp	Pucangan Formation		
			Gelasian				
Neogene	Pliocene	Upper	Piacenzian	Tmpk	Kalibeng Formation	Tpkk	Klitik Member
		Lower	Zanclean			Tmkk	Kapung Member
	Miocen	Upper	Messinian			Tmkb	Banyak Member
			Tortonian				
		Middle	Serravalian	Tmk	Kerek Formation		
			Langhian				

Figure 1. Regional geological map of the research area and the location of 2 soil profiles. Geological map from Sukardi & Budhitrisna (1992)

The X-ray diffraction (XRD) bulk analysis is a critical method for determining the crystal mineral composition and crystalline structure of materials, which involves several key stages. Initially, the sample was grinded to finely ground to ensure homogeneity and optimal diffraction. Following this, the XRD measurement is conducted, where the sample is exposed to X-rays, and the diffraction pattern is recorded. This pattern is then analyzed to identify the mineral types present, utilizing databases from (Anthony et al., 2010). For semi-quantitative mineral composition analysis, the relative intensities of the diffraction peaks are compared, allowing for the estimation of the proportion of each mineral phase. Additionally, the degree of crystallinity is assessed using the Full Width at Half Maximum (FWHM) values of the peaks, which provide insights into the crystallite size and structural disorder.

Thin section petrography analysis under a polarization microscope involves several systematic steps. First, a thin section of the tuff sample 30 microns thick is prepared and mounted on a glass slide. The slide is then placed on the stage of a polarizing light microscope, which is equipped with both plane-polarized (PPL) and cross-polarized (XPL) light settings. The analysis begins with an initial observation in PPL, where the color, relief, and transparency are evaluated. Next, the sample is examined under XPL by rotating the upper polarizer, which helps in identifying optical properties such as birefringence, interference colors, extinction angles, and twinning. By systematically rotating the stage and switching between PPL and XPL, the observer can distinguish and identify minerals based on their diagnostic optical features. Observations are typically recorded, and mineral or glass proportions, grain sizes, textures, and relationships are documented for further interpretation.

Mathematical equation:

$$1\,m = \left(\frac{c}{299\,792\,458}\right) s = \frac{9\,192\,631\,770}{299\,792\,458}\frac{c}{\Delta\nu^{cs}} \approx 30.663\,319\,\frac{c}{\Delta\nu^{cs}}$$

RESULTS AND DISCUSSION

Geology of Notopuro Formation

The Notopuro Formation marks the final depositional phase in the Sangiran Dome during the Late Pleistocene, characterized by coarse volcaniclastic deposits like lahars and pyroclastic flows, interspersed with fluvial sands. This increase in volcanic material suggests heightened regional tectonic activity, possibly linked to the Kendeng Hills uplift. Paleoenvironmental evidence, including calcic paleosols and xerophytic pollen, points to a drier climate than that of the underlying Kabuh Formation (Bettis et al., 2009). Although hominin fossils are scarce, stone tools in reworked deposits indicate their continued presence. Dated to around 0.1 Ma, the upper Notopuro layers conclude the Sangiran sedimentary record before regional uplift and erosion (Hyodo et al., 2011).

The Notopuro Formation is characterized by abundant volcaniclastic deposits exhibiting clear sedimentological markers. Pyroclastic flow deposits are composed of 60-80% volcanic lithics, whereas lahars contain andesitic clasts measuring up to 30 cm in diameter. Palynological data indicate a substantial reduction in humidity-dependent taxa, accounting for less than 20% of total pollen, which aligns with prevailing regional aridification. Fossil teeth display oxygen isotope values that are 2.3‰ higher than those from the Kabuh Formation, further substantiating the presence of drier climatic conditions. Analysis of dental microwear patterns in *Elephas hysudrindicus* reveals distinct grit abrasion, suggesting exposure to dusty environments (Meralli, 2025). The geological map of the study site is shown in Figure 1.

Soil morphology

A general observation suggests that both sampling locations exhibit similarities. The similarity observed is that both locations exhibit less distinct soil horizon differentiation characteristics. A general observation of the differences in horizons reveals that these are only present in the form of soil layers, parent material, or weathered rock, followed by bedrock. The observed soil structure is characterized by a multitude of cracks that are dark brown in color. When subjected to a process of hydration and subsequent friction, the material exhibits a texture that is notably slippery, reminiscent of soap. These signs are one indication of the presence of smectite clay minerals. When correlated with a soil structure that has many fractures, it can be tentatively concluded that these cracks are caused by the swelling and shrinking activity of smectite minerals. Photographic representations of soil profiles from both locations are presented in Figure 2. The following paragraphs provide a more detailed explanation of the two soil profiles.

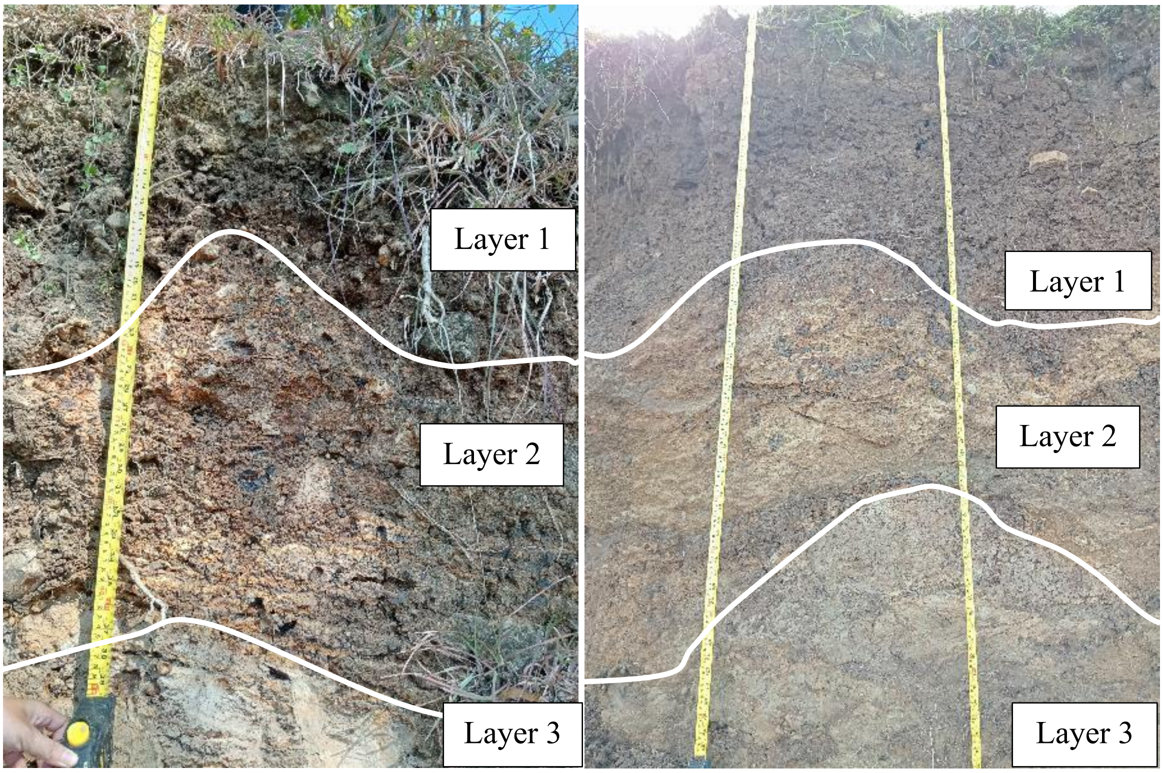

Figure 2. Soil profiles developed from Notopuro Tuff. The right picture shows Profile 1 and the left picture shows Profile 2.

Soil profile 1 has a thickness of layer 1, which is a soil layer with a thickness of 50 cm. Layer 2 is the parent material layer consisting of disintegrated bedrock material that has changed color to light brown. The thickness of layer 2 is also 50 cm. Although layer 2 has undergone disintegration and color change, it does not yet exhibit significant plastic characteristics like layer 1. The hardness remains relatively similar to the layer below it. Furthermore, layer 3 is the bedrock layer that appears only slightly weathered. It has a gray color and exhibits hard physical characteristics similar to rock.

In the second soil profile, layer 1 (soil) is thicker compared to profile 1, measuring 90 cm. Layer 2 has a thickness of 40 cm. Layer 2 in this profile shows a more advanced degree of weathering compared to layer 2 in profile 1. It consists of blocks and clumps of weathered rock that are plastic and not hard, with a light brown color. Numerous cracks filled with clay material are found. Layer 3 also exhibits characteristics of having weathered, being neither hard nor sufficiently plastic.

Table 1. Bedrock profile 1 layer 3 oxide composition based on SEM EDS

Oxide	%wt	%molar
Na_2O	0.00	0.00
MgO	9.75	14.75
Al_2O_3	12.01	7.18
SiO_2	56.40	57.24
K_2O	0.00	0.00
CaO	9.88	10.75
TiO_2	0.92	0.70
FeO(T)	11.04	9.37
Na_2O+K_2O	0.00	n/a
FeO(T)/(FeO(T)+MgO)	0.53	n/a
Na_2O+K_2O-CaO	-9.88	n/a
$Al_2O_3/(Na_2O+K_2O)$	n/a	approaching infinite
$Al_2O_3/(CaO+Na_2O+K_2O)$ (ASI)	n/a	0.67

Remarks:
Normalized oxide composition in anhydrous
n/a = not applicable

Tuff geochemistry and mineralogy

Geochemical analysis of the tuff was restricted to samples from Location 1, Layer 3. These samples were the freshest and did not exhibit any signs of weathering. This argument is further strengthened by its relatively low weathering index value (Table 5) and also this is further strengthened through ternary diagrams (Babechuk & Fedo, 2023) (Figure 5), where the resulting plots fall within the range of unweathered rocks. This is because geochemical analysis for rocks is only valid if the rock samples have not undergone weathering.

The results of the oxide composition analysis in mass percent and molar percent can be seen in Table 1. Based on Table 1, the ratios of several oxides can be observed. From the plot of %wt SiO_2 and %K_2O on Ewart (1982) curve and %wt Na_2O+K_2O on Le Bas et al. (1986) curve, it is estimated that the tuff at the study site originated from a magma with basaltic andesite and low-K affinity. Considering the plot of %wt SiO_2 values along with %wt (Na_2O+K_2O-CaO) and the ratio %wt FeO(T)/(FeO(T)+MgO) by (Frost et al., 2001), it is found that the tuff samples from the study site originated from a calcic and magnesian magma. Furthermore, according to the alumina saturation index (ASI) classification by (Shand, 1927), based on the plot of %molar $Al_2O_3/(Na_2O+K_2O)$ and $Al_2O_3/(CaO+Na_2O+K_2O)$, the level of alumina saturation is determined to be metaluminous.

The mineral composition of the tuff sample was analyzed using thin section observations under a polarizing microscope. Thin section observations were conducted on layers 2 and 3 of both profiles. The four samples exhibited different texture and structural characteristics. There were differences in the mineral composition of the four samples. Nevertheless, all four samples were predominantly composed of volcanic glass and lithic fragments. The information of the thin section observation results can be seen in Table 2 and Figure 3. The lithological naming of the four samples was based on the classification by Schmid (1981).

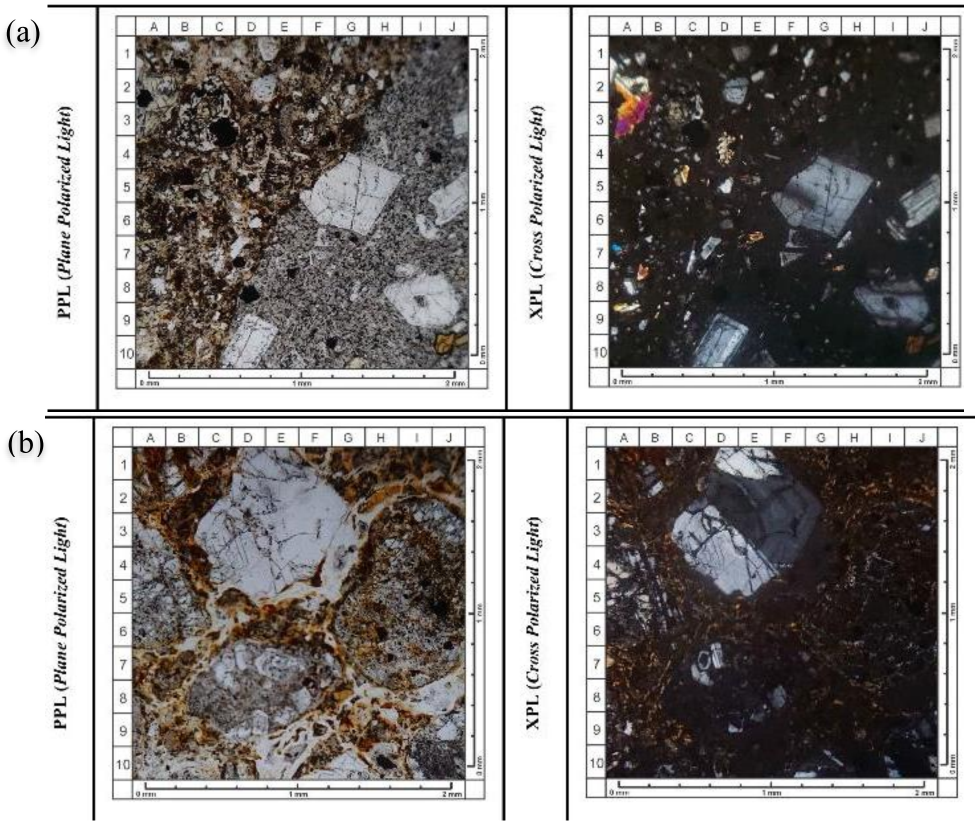

Figure 3. Thin section petrography from Notopuro Tuff sample: (a) Profile 1 Bedrock, (b) Profile 2

Table 2. Mineral, glass, and lithic fragment composition of the bedrock based on petrographic thin sections in percent

Mineral/Glass	Profile 1	Profile 2
Lithic Fragment	50	30
Feldspar	3	15
Quartz	2	1
Hornblende	Lit	Lit
Clinopyroxene	Lit	Lit
Orthopyroxene	4	Lit
Volcanic Glass	39	53
Opaque	2	1
Total	100	100

Remarks: Lit = present in lithic fragment

The bedrock of Profile 1 observed with an ocular magnification of 10x and an objective magnification of 5x shows a massive structure, with a texture comprising grain sizes of <1/256 – >2 mm, poor sorting, and open packing. The composition is dominated by lithic fragments, with a significant amount of volcanic glass. Other detected minerals include feldspar, quartz, and orthopyroxene. The lithological name is lithic tuff. The bedrock of profile 2 observed with an ocular magnification of 10x and an objective magnification of 5x shows a massive structure, with a texture comprising grain sizes of <1/256 – 1 mm, moderate sorting, and open packing. It is dominated by volcanic glass with a considerable number of lithic fragments and feldspar. There is a small amount of quartz mineral. Its lithological name is vitric tuff.

Geochemistry and weathering characteristics of residual soil

The results of the oxide composition analysis of the test samples can be found in Table 3 and Table 4. Manganese oxide is assumed to have a valence of +2, while iron valence is assumed to be +3, in accordance with the analytical requirements of this subsection. The results of the weathering degree analysis using the IOL/IOB can be seen in Table 3, and the weathering degree using the CIA and MIA methods can be seen in Table 4. The chosen MIA parameter is MIA assuming oxidative conditions (MIA (O)) because the resulting soil color tends to be brown with a slight reddish hue. According to Babechuk et al. (2014), this is sufficient to indicate that the weathering process is occurring under oxidative conditions, thus, MIA (O) can be selected. Detailed explanations regarding the interpretation of weathering intensity will be elaborated in the subsequent paragraphs.

Based on the CIA and MIA(O) values, it was found that there are generally differences in the weathering degree change patterns between the two profiles. The plot of the changes in CIA and MIA(O) values against soil horizons from both profiles can be seen in Figure 4. Profile 1 shows an intense increase in weathering from horizon 3 to 2, but only shows a slight increase from horizon 2 to 1. This pattern is consistent for both CIA and MIA(O). Conversely, Profile 2 shows a less intense change in weathering degree from horizon 3 to 2, but from horizons 2 and 1, it shows an intense change in weathering degree according to CIA. However, when viewed from the MIA(O) values, the change in weathering degree is relatively linear. The soil sample that has undergone the most intense weathering is the sample from horizon 1 of Profile 2, with a CIA value of 93.4 and an MIA(O) of 89.11. With CIA values greater than 90, classification using CIA or MIA is no longer appropriate, thus requiring weathering classification using IOL according to Babechuk et al. (2014) classification.

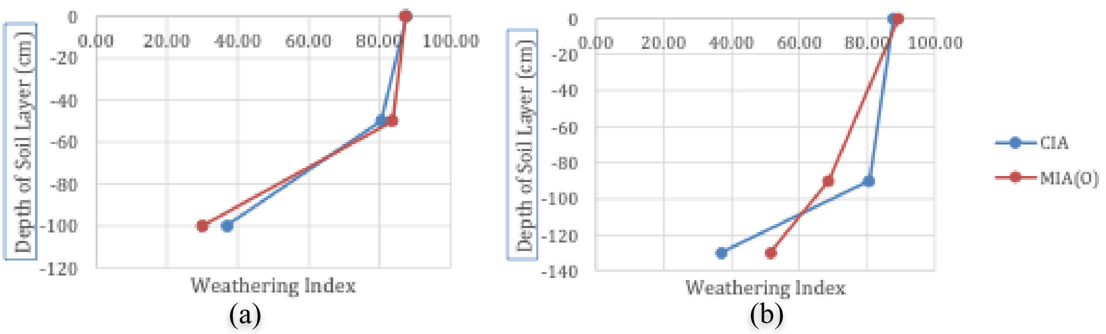

Figure 4. Plot of chemical weathering index values against depth of soil layers from (a) Profile 1 and (b) Profile 2

According to Babechuk et al. (2014), CIA and MIA values can either be correlated or uncorrelated. Based on the data from this study's sample, correlation and linear regression analyses were conducted between the obtained CIA and MIA(O) values. The results of the correlation and linear regression analyses yielded several key points: (a) the Pearson correlation coefficient (r) was 0.98 (high), (b) the significance (F) of the linear regression equation was 0.00079 (F>0.05), (c) the P-values for the intercept and the slope of the straight line (CIA coefficient) were 0.42 (P-value > 0.05) and 0.00079 (P-value < 0.05), respectively, and (d) the regression equation was MIA(O) = 1.08761 CIA – 7.81593. It can be concluded that although numerous statistical parameters indicate a strong linear correlation between CIA and MIA(O) in the test sample, the resulting intercept value has a P-value > 0.05. Therefore, it can be concluded that there is a correlation between CIA and MIA(O) values in the test sample, but with exceptions in some samples. When linked to the original CIA and MIA(O) values, profile 2 indeed exhibits a different pattern of CIA and MIA(O) value changes. The CIA formula itself measures the molar percentage change of Al_2O_3 relative to Al_2O_3, CaO, Na_2O, and K_2O, while MIA(O) measures the molar percentage change of Al_2O3 and Fe_2O_3 relative to Al_2O_3, Fe_2O_3, MgO, CaO, Na_2O, and K_2O. Consequently, CIA fundamentally does not measure changes in ferric, magnesium, and calcium oxides. In profile 2, the percentage changes in ferric, magnesium, and calcium oxides are relatively greater compared to profile 1. This results in relatively similar CIA and MIA(O) values and aligned changes in profile 1. Meanwhile, in profile 2, the CIA and MIA(O) values become more disparate, and their value change patterns also differ.

Table 3. Soil and tuff oxide composition in percent mass

No	Oxide	Profile 1			Profile 2		
		Layer 1	Layer 2	Layer 3	Layer 1	Layer 2	Layer 3
	Depth (cm)	0 - 50	50 - 100	> 100	0 - 90	90 - 130	> 130
1	Na_2O	0.17	1.82	0.00	0.00	1.62	1.79
2	MgO	0.59	0.00	9.77	1.06	1.64	4.57
3	Al_2O_3	28.02	29.67	10.57	29.09	12.31	23.18
4	SiO_2	51.96	53.00	56.53	51.53	48.95	52.67
5	K_2O	0.00	0.99	0.00	0.00	0.81	0.10
6	CaO	2.02	1.71	9.91	1.13	2.05	7.24
7	TiO_2	1.62	0.46	0.92	2.05	13.11	0.55
8	MnO(T)	0.31	1.20	0.00	0.00	0.00	0.00
9	Fe_2O_3(T)	14.83	11.15	12.30	15.14	19.53	9.89
10	ZrO_2	0.47	0.00	0.00	0.00	0.00	0.00
	IOL/IOB	45.20	43.51	28.80	46.19	39.41	38.57

Remarks: Normalized oxide composition in anhydrous

The IOL/IOB value for layer 1 of profile 2 was obtained as 46.19. This IOL/IOB value does not actually indicate an intense weathering process. However, it should be noted that IOL/IOB measures the percentage change in mass of Al_2O3 and Fe_2O_3 relative to SiO_2, Al_2O_3, and Fe_2O_3. In other words, a high IOL/IOB value (considered intense weathering) requires a significant loss of SiO_2. This process is referred to as lateritization for Fe_2O_3 enrichment and bauxitization for Al_2O_3 enrichment, so IOL/IOB actually measures the degree of lateritization or bauxitization of the soil (Babechuk et al., 2014;

Babechuk & Fedo, 2023; Broz et al., 2025; Irzon et al., 2021). Therefore, it can be concluded that the soil test samples have undergone intense weathering according to CIA and MIA(O) through the mobilization mechanism of their alkali and alkaline earth oxides, but the lateritization process has not yet been intense (SiO_2 has only undergone minor mobilization). According to Babechuk et al. (2014), this process is called kaolinitization. Based on the SAF ternary diagram plot (Figure 5), the samples from layer 1 of profile 2 have undergone kaolinitization. The other samples also only reached the kaolinitization stage (did not experience lateritization).

Table 4. Soil and tuff oxide composition in molar ratio

No	Oxide	Profile 1			Profile 2		
		Layer 1	Layer 2	Layer 3	Layer 1	Layer 2	Layer 3
	Depth (cm)	0 - 50	50 - 100	> 100	0 - 90	90 - 130	> 130
1	Na_2O	0.003	0.029	0.000	0.000	0.026	0.029
2	MgO	0.015	0.000	0.242	0.026	0.041	0.113
3	Al_2O_3	0.275	0.291	0.104	0.285	0.121	0.227
4	SiO_2	0.865	0.882	0.941	0.858	0.815	0.877
5	K_2O	0.000	0.011	0.000	0.000	0.009	0.001
6	CaO	0.036	0.030	0.177	0.020	0.037	0.129
7	TiO_2	0.020	0.006	0.012	0.026	0.164	0.007
8	MnO(T)	0.004	0.017	0.000	0.000	0.000	0.000
9	Fe_2O_3(T)	0.093	0.070	0.077	0.095	0.122	0.062
10	ZrO_2	0.004	0.000	0.000	0.000	0.000	0.000
	CIA	87.68	80.54	36.97	93.40	62.90	58.82
	MIA(O)	87.33	83.69	30.12	89.11	68.49	51.48

Remarks: Normalized oxide composition in anhydrous

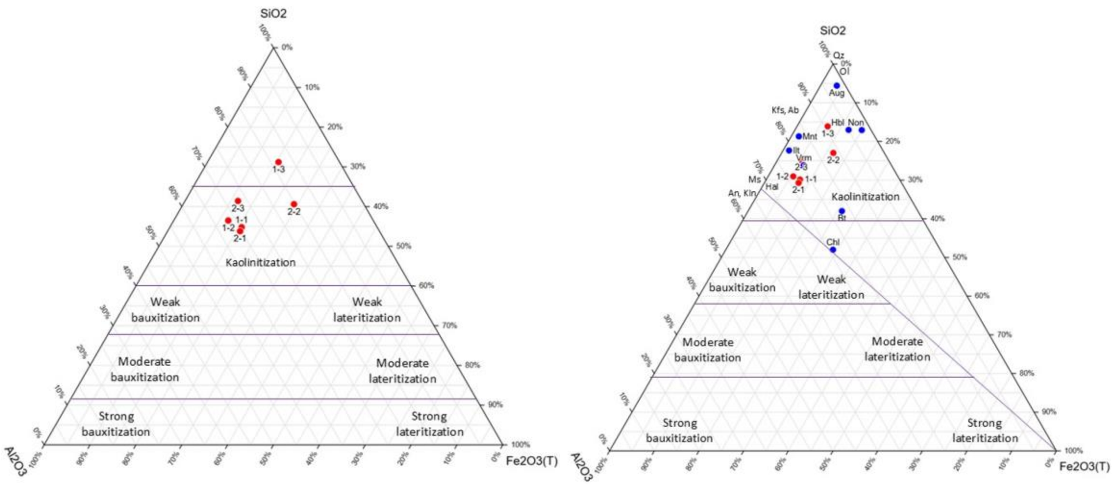

Figure 5. Mass SiO_2–Al_2O_3–Fe_2O_3(T) (SAF) ternary plots of test specimens. (a) Ternary diagram using %wt, and (b) Ternary diagram using molar percent and supplemented with typical values of several mineral types (blue dots). Red dots represent values for test samples, with the first number indicating the profile number and the second number indicating the layer sequence. Ternary diagram from Babechuk & Fedo (2023).

Soil mineralogy

The crystal mineral composition of the soil sample was analyzed using XRD. XRD observations were conducted on layer 1 of Profile 1 and all layers in Profile 2. In general, all four XRD test samples exhibit nearly identical mineral compositions with only minor differences. Based on bulk XRD analysis, all four test samples are dominated by feldspar minerals. Other minerals found in significant quantities in all four samples include quartz and cristobalite. The complete results of the mineral analysis using bulk XRD can be found in (Table 5). Upon observation of profile 2, several minerals were found to exhibit alteration tendencies that correlate with changes in the degree of weathering. The minerals that clearly demonstrate this alignment of their abundance trends with weathering are augite, faujasite, lepidocrocite, quartz, and smectite. Augite and lepidocrocite show a linear decrease in abundance with increasing weathering intensity, while smectite exhibits the opposite trend. Faujasite and feldspar other than microcline displays a steeper decline in abundance as the degree of weathering increases. Meanwhile, microcline and quartz show a highly significant increase in abundance with advancing weathering. It can be concluded, based on the increase in weathering rates, that the minerals experiencing a decrease in concentration are augite, lepidocrocite, faujasite, and feldspar (excluding microcline), whereas those showing an increase in concentration are microcline, quartz, and smectite.

Table 5. Mineralogical composition of the soils based on bulk XRD analysis

No	Mineral	Profile 1		Profile 2	
		Layer 1	Layer 1	Layer 2	Layer 3
	Depth (cm)	0 - 50	0 - 90	90 - 130	> 130
1	Anatase	+	+	+	+
2	Augite	++	-	+	+
3	Cristobalite	+++	++	+	++
4	Faujasite	+	-	+	+++
5	Ferro-Ferri Hornblende	-	-	++	-
6	Other Feldspar	++	-	+++	+++
7	Hematite	+	+	-	+
8	Kaolinite	+	+	+	+
9	Lepidocrocite	-	-	+	+
10	Magnetite	+	++	+	++
11	Microcline	+++	++++	+	+
12	Quartz	+	+++	++	+
13	Smectite	-	+	+	-

Remarks: - = none, + = little, ++ = medium, +++ = enough, ++++ = many

The FWHM analysis results for the detected mineral crystal peaks in the XRD test samples can be observed in Table 6. Based on Table 6, it is evident that the FWHM values range from 0.2007° to 1.0706°. The majority of the detected mineral crystals exhibit an FWHM value of 0.2007°. The minerals with the largest FWHM are smectite and anatase originating from profile 1, layer 1. In general, a large FWHM value indicates a poor degree of crystallinity, and conversely, a smaller FWHM value indicates a better degree of crystallinity. When reviewed from the pattern of FWHM change with increasing weathering degree, there are minerals whose FWHM values decrease and also increase.

Minerals with decreasing FWHM values are augite, feldspar other than microcline, and kaolinite, with a relatively linear rate of decrease. Meanwhile, those with increasing FWHM are anatase, cristobalite, hematite, and lepidocrocite, with a higher rate of change compared to the minerals whose FWHM decreases. Nevertheless, the classification of FWHM values and the determination of the degree of crystallinity for each mineral species have diverse methods and thresholds.

Table 6. FWHM value of crystal mineral composition of the soils based on bulk XRD analysis in degree

No	Mineral	FWHM			
		Profile 1	Profile 2		
		Layer 1	Layer 1	Layer 2	Layer 3
	Depth (cm)	0 – 50	0 - 90	90 - 130	> 130
1	Anatase	1.07	0.67	0.20	0.20
2	Augite	0.20	n.d.	0.20	0.27
3	Cristobalite	0.20	0.80	0.20	0.20
4	Faujasite	0.20	n.d.	0.20	0.20
5	Ferro-Ferri Hornblende	n.d.	n.d.	0.20	n/a
6	Other Feldspar	0.20	n.d.	0.27	0.33
7	Hematite	0.54	0.54	n.d.	0.20
8	Kaolinite	0.67	0.47	0.67	0.94
9	Lepidocrocite	n.d.	n.d.	0.40	0.20
10	Magnetite	0.46	0.40	0.27	0.40
11	Microcline	0.40	0.37	0.54	0.33
12	Quartz	0.40	0.20	0.20	0.20
13	Smectite	n.d.	1.07	1.07	n.d.

Remarks: n.d. = not detected

Tuff basaltic andesite, characterized as lithic-crystal-vitric tuff with nearly equal proportions of components. These pyroclastic materials originate from the eruption of the Ancient Ungaran Volcano, which is located to the west of the Notopuro Formation deposits (Kusumayudha et al., 2011). The strongest interpretation for the lithic-rich (yet balanced with juvenile material) basaltic andesite tuff points towards a Vulcanian-type eruption. This eruptive mechanism is characterized by the ascent of new, juvenile magma being impeded by a pre-existing, solidified plug or lava barrier within the conduit (lithics). Consequently, the pressure from accumulating volcanic gases intensifies until it violently expels this obstruction. Evidence from volcanic deposits in New Zealand and the Andes supports this, as coarse, crystal- and lithic-rich tuff facies frequently represent "vent clearing episodes" (Prentice et al., 2020). The lithic fragments observed originate from the fractured conduit walls or the dislodged plug, while the juvenile fragments and crystals are derived from the fresh magma that initiated and drove the explosive event. This compositional signature, therefore, is a direct indicator of the explosive interaction between ascending juvenile magma and a solidified conduit blockage, a hallmark of Vulcanian activity (Kudo, 2024). Research related to eruption models of Mount Ungaran has not been extensively conducted, therefore, it is expected that further research will be undertaken. Further research aims to develop an eruption model for Mount Ungaran based on the characterization of rocks from the Notopuro Formation. This will involve a larger sample size that is representative of the entire lithology present in the Notopuro Formation, thereby leading to a more accurate resultant model.

In general, the geochemical characteristics of the Notopuro Tuff samples with the lava and magma of Mount Ungaran, based on research by (Suhendro et al., 2023), do not exhibit significant differences except for the K element. The lava and magma of Mount Ungaran tend to be K-rich, contrasting with the K-poor Notopuro tuff samples. This phenomenon is quite common and can be attributed to the K leaching process by water. When tuff is exposed to water (rainwater, groundwater, or seawater), volcanic glass undergoes hydrolysis. Large Ion Lithophile Elements (LILE) such as Potassium (K), Sodium (Na), and Calcium (Ca) are highly soluble in water and detach from the glass structure. Conversely, immobile elements like Titanium (Ti), Zirconium (Zr), and Aluminum (Al) tend to remain. K-rich volcanic glass (as in High-K Basaltic Andesite) will alter into clay minerals such as smectite, kaolinite, or halloysite. These clay minerals possess a crystal structure incapable of accommodating as much K as the original glass, leading to K loss in the leachate (Fan et al., 2020; Li et al., 2022). Meanwhile, if the tuff is deposited far from its original volcano (as in this sample), eolian fractionation processes can occur. If wind separates K-rich glass (carried further as fine dust) and leaves behind K-poor plagioclase crystals (falling closer as coarse tuff), then chemical analysis of the coarse tuff will show low K content, even if the magma is High-K (Dominguez et al., 2020). It can be concluded that the loss of K in the Notopuro tuff is caused by water leaching processes as well as eolian processes.

The weathered tuff layer of Notopuro has undergone intensive chemical weathering but has not undergone lateritization. Kaolinitization and lateritization processes fundamentally represent two distinct weathering stages where kaolinitization signifies early to intermediate weathering stages, and lateritization represents a final stage weathering process. Kaolinitization is characterized by the transformation of primary minerals through the hydrolysis of primary silicate minerals into secondary silicate minerals. Si is largely retained within the phyllosilicate structure, indicated by a still relatively high SiO_2 percentage (Babechuk & Fedo, 2023). Meanwhile, the subsequent process, lateritization, involves intense desilication. Si becomes leached out, leaving behind only sesquioxide minerals such as gibbsite, goethite, and hematite (Babechuk & Fedo, 2023). The lateritization process requires high rainfall (>2000 mm/year) and constant tropical temperatures (25°C) (Li et al., 2016). Regarding weathering duration, lateritization generally takes longer than 100,000 years, while kaolinitization only requires between 10,000 to 100,000 years (Babechuk & Fedo, 2023). The Notopuro Formation was formed during the Late Pleistocene (129,000 to 11,700 years ago), thus having a low probability of undergoing lateritization. Furthermore, excellent vertical drainage is required for intensive Si leaching, where tuff generally possesses high porosity, creating lateral drainage that prevents vertical leaching, preserves Si saturation, and inhibits lateritization or bauxitization (Dubroeucq et al., 1998). Thus, it can be concluded that the incomplete laterization or bauxitization process in the Notopuro tuff residual soil is attributed to the young age of the bedrock and its porous characteristics, which prevent the leaching of Si.

Based on the mineral analysis results of profile 2, it was found that minerals experiencing decreased concentration due to increased weathering include augite, faujasite, lepidocrocite, and feldspar excluding microcline. Considering their resistance to weathering, these minerals are relatively susceptible to weathering. From the list above, faujasite is the least stable mineral against weathering, as faujasite tends to undergo framework structure disintegration at weathering temperatures (Guan et al., 2019). The dissolution rates of other minerals can be seen in Table 7. Based on Table 7, a sequence of mineral weathering susceptibility can be concluded based on their dissolution rate values, namely: (1) faujasite, (2) Ca-plagioclase, (3) lepidocrocite, (4) augite, (5) albite, (6) smectite, (7) microcline, and (8) quartz. Due to their relatively more resistant nature to weathering, microcline and quartz can still persist in the weathered tuff layer. Meanwhile, smectite is an alteration product of volcanic glass, where increased weathering intensity will lead to more volcanic glass weathering and transformation into smectite (Deer et al., 2013).

Table 7. Average Dissolution rates of some minerals in a tropical climate weathering environment. Minerals are ordered from most to least soluble

No	Minerals	Average Dissolution Rates $mol.cm^{-2}s^{-1}$	References
1	Faujasite	Framework collapse at room temperature	(Castro et al., 2019; Guan et al., 2019)
2	Plagioclase (Ca-rich)	10^{-12}	(de Obeso et al., 2023)
3	Lepidocrocite	$5,8 \times 10^{-14}$	(Biswakarma et al., 2020)
4	Augite	$10^{-14.8}$	(Monasterio-Guillot et al., 2021; Schott & Berner, 1985)
5	Plagioclase (albite)	3×10^{-15}	(Gudbrandsson et al., 2014)
6	Smectite	2×10^{-15}	(Amram & Ganor, 2005; Brantley et al., 2023)
7	Microcline	3×10^{-16}	(Lin et al., 2023)
8	Quartz	10^{-21} - 10^{-20}	(Gong et al., 2022)

The FWHM values of the detected mineral crystals in the weathered tuff material of Notopuro range from 0.20° to 1.07°. Generally, this range of values indicates a relatively low degree of crystallinity (greater than 0.2°) (Elong et al., 2023; Londoño-Restrepo et al., 2019; Warr, 2018). This is actually quite common in many types of residual soils. Nevertheless, resistant minerals such as quartz generally can still exhibit low FWHM values (Jannat et al., 2025; Karlinasari et al., 2023; Zadvernyuk et al., 2021). In this test sample, the detected quartz mineral has an FWHM value of 0.2007°, which is already considered to have a poor degree of crystallinity. This can be attributed to the presence of quartz crystals being a mixture of detrital quartz with a microcrystalline SiO_2 phase. This mixture, when read by XRD, will produce a slightly broadened peak at the 2θ value of 26.6° (Locati et al., 2022). This microcrystalline SiO_2 originates from the weathering of volcanic glass, which releases Si into the soil solution, subsequently re-precipitating as secondary quartz (Latif et al., 2016).

When compared to the mineral composition of weathered volcanic rocks with similar geochemical characteristics (basaltic andesite), the weathered tuff of Notopuro exhibits mineralogical similarities to basaltic andesite in several other locations in Indonesia. Minerals that are also found in weathered basaltic andesite rocks include quartz, augite, hornblende, and feldspar (Muslim et al., 2020). The minerals detected in the Notopuro tuff and its weathered products exhibit similarities to the mineral composition of the pyroclastic deposits of Lawu, located to the southeast and bounded by the Bengawan Solo River deposits (Nurcholis et al., 2019).

CONCLUSION

Tuff at the study site originated from a magma with basaltic andesite, low-K affinity, calcic and magnesian magma. The level of alumina saturation is determined to be metaluminous. The tuff composition is dominated by lithic fragments (50%) with significant volcanic glass (39%). In general, the weathering characteristics observed in the tuff at the research site involve enrichment of Al_2O_3 and Fe_2O_3, with the Fe_2O_3 enrichment process exhibiting a more intense profile. SiO_2 tends to remain relatively unchanged in the weathered soil, indicating that the degree of tuff weathering at the research site has only reached the kaolinitization stage and has not yet undergone lateritization or bauxitization. The mineral fraction found in the weathered tuff is dominated by microcline and quartz, with significant amounts of cristobalite and magnetite. The detected mineral crystallinity tends to be low.

REFERENCES

Amram, K., & Ganor, J. (2005). The combined effect of pH and temperature on smectite dissolution rate under acidic conditions. *Geochimica et Cosmochimica Acta*, *69*(10), 2535–2546. https://doi.org/10.1016/j.gca.2004.10.001

Anthony, J. W., Bideaux, R. A., Bladh, K. W., & Nichols, M. C. (2010). *Handbook of Mineralogy*. Mineralogical Society of America.

Babechuk, M. G., & Fedo, C. M. (2023). Analysis of chemical weathering trends across three compositional dimensions: applications to modern and ancient mafic-rock weathering profiles. *Canadian Journal of Earth Sciences*, *60*(7), 839–864. https://doi.org/10.1139/cjes-2022-0053

Babechuk, M. G., Widdowson, M., & Kamber, B. S. (2014). Quantifying chemical weathering intensity and trace element release from two contrasting basalt profiles, Deccan Traps, India. *Chemical Geology*, *363*, 56–75. https://doi.org/10.1016/j.chemgeo.2013.10.027

Bettis, E. A., Milius, A. K., Carpenter, S. J., Larick, R., Zaim, Y., Rizal, Y., Ciochon, R. L., Tassier-Surine, S. A., Murray, D., Suminto, & Bronto, S. (2009). Way out of Africa: Early Pleistocene paleoenvironments inhabited by Homo erectus in Sangiran, Java. *Journal of Human Evolution*, *56*(1), 11–24. https://doi.org/10.1016/j.jhevol.2008.09.003

Bhavya, K., & Nagaraj, H. B. (2025). Influence of soil structure and clay mineralogy on Atterberg limits. *Scientific Reports*, *15*(1), 15459. https://doi.org/10.1038/s41598-025-98729-y

Biswakarma, J., Kang, K., Schenkeveld, W. D. C., Kraemer, S. M., Hering, J. G., & Hug, S. J. (2020). Linking isotope exchange with Fe(II)-Catalyzed dissolution of Iron(hydr)oxides in the presence of the bacterial siderophore Desferrioxamine-B. *Environmental Science & Technology*, *54*(2), 768–777. https://doi.org/10.1021/acs.est.9b04235

Brantley, S. L., Shaughnessy, A., Lebedeva, M. I., & Balashov, V. N. (2023). How temperature-dependent silicate weathering acts as Earth's geological thermostat. *Science*, *379*(6630), 382–389. https://doi.org/10.1126/science.add2922

Broz, A. P., Horgan, B. H. N., Bedford, C., Royer, C., Manelski, H., Connell, S., Wiens, R. C., Cardarelli, E. C., Madariaga, J. M., Mandon, L., Klidaras, A., Bramble, M., Kathir, B., Forni, O., Carter, J., Dehouck, E., Quantin-Nataf, C., Johnson, J. R., Nuñez, J. I., … Cousin, A. (2025). Alteration history of aluminum-rich rocks at Jezero crater, Mars. *Communications Earth & Environment*, *6*(1), 935. https://doi.org/10.1038/s43247-025-02856-3

Castro, P. R. dos S. de, Maia, A. Á. B., & Angélica, R. S. (2019). Study of the thermal stability of faujasite zeolite synthesized from kaolin waste from the Amazon. *Materials Research*, *22*(5). https://doi.org/10.1590/1980-5373-mr-2019-0321

de Obeso, J. C., Awolayo, A. N., Nightingale, M. J., Tan, C., & Tutolo, B. M. (2023). Experimental study on plagioclase dissolution rates at conditions relevant to mineral carbonation of seafloor basalts. *Chemical Geology*, *620*, 121348. https://doi.org/10.1016/j.chemgeo.2023.121348

Deer, W. A., Howie, R. A., & Zussman, J. (2013). *An Introduction to the Rock-Forming Minerals*. Mineralogical Society of Great Britain and Ireland. https://doi.org/10.1180/DHZ

Dominguez, L., Bonadonna, C., Forte, P., Jarvis, P. A., Cioni, R., Mingari, L., Bran, D., & Panebianco, J. E. (2020). Aeolian remobilisation of the 2011-Cordón Caulle Tephra-Fallout Deposit: example of an important process in the life cycle of volcanic ash. *Frontiers in Earth Science*, *7*. https://doi.org/10.3389/feart.2019.00343

Dubroeucq, D., Geissert, D., & Quantin, P. (1998). Weathering and soil forming processes under semi-arid conditions in two Mexican volcanic ash soils. *Geoderma*, *86*(1–2), 99–122. https://doi.org/10.1016/S0016-7061(98)00033-0

Elong, K., Kasim, M. F., & Osman, Z. (2023). Effect of titanium doping on structure and morphology of LiNi0. 3Mn0. 3Co0. 3Al0. 1O2 Cathode Materials. In M. F. Malek, N. A. Asli, & M. H. F. Suhaimi (Eds.), *13th Nanoscience and Nanotechnology Conference Proceeding* (pp. 75–82). https://doi.org/10.4028/p-aj1ep5

Ewart, A. (1982). The Mineralogy and petrology of Tertiary-Recent orogenic volcanic rocks; with special reference to the andesitic-basaltic compositional range. *Andesites: Orogenic Andesites and Related Rocks*, 26–87.

Fan, C., Li, H., Qin, Q., Shang, L., Yuan, Y., & Li, Z. (2020). Formation mechanisms and distribution of weathered volcanic reservoirs: A case study of the carboniferous volcanic rocks in Northwest Junggar Basin, China. *Energy Science & Engineering*, *8*(8), 2841–2858. https://doi.org/10.1002/ese3.702

Frost, B. R., Barnes, C. G., Collins, W. J., Arculus, R. J., Ellis, D. J., & Frost, C. D. (2001). A Geochemical Classification for Granitic Rocks. *Journal of Petrology*, *42*(11), 2033–2048. https://doi.org/10.1093/petrology/42.11.2033

Gong, K., Aytas, T., Zhang, S. Y., & Olivetti, E. A. (2022). Data-driven prediction of quartz dissolution rates at near-neutral and alkaline environments. *Frontiers in Materials*, *9*. https://doi.org/10.3389/fmats.2022.924834

Guan, L., Wang, Z., & Lu, D. (2019). Evolution of zeolite crystals in self-supporting faujasite blocks: effects of hydrothermal conditions. *Materials*, *12*(12), 1965. https://doi.org/10.3390/ma12121965

Gudbrandsson, S., Wolff-Boenisch, D., Gislason, S. R., & Oelkers, E. H. (2014). Experimental determination of plagioclase dissolution rates as a function of its composition and pH at 22°C. *Geochimica et Cosmochimica Acta*, *139*, 154–172. https://doi.org/10.1016/j.gca.2014.04.028

Hyodo, M., Matsu'ura, S., Kamishima, Y., Kondo, M., Takeshita, Y., Kitaba, I., Danhara, T., Aziz, F., Kurniawan, I., & Kumai, H. (2011). High-resolution record of the Matuyama–Brunhes transition constrains the age of Javanese *Homo erectus* in the Sangiran dome, Indonesia. *Proceedings of the National Academy of Sciences*, *108*(49), 19563–19568. https://doi.org/10.1073/pnas.1113106108

Indrawan, I. G. B., Tamado, D., Abrar, M., & Warmada, I. W. (2024). Mineralogical and engineering properties of soils derived from in situ weathering of tuff in Central Java, Indonesia. *Geosciences*, *14*(8), 213. https://doi.org/10.3390/geosciences14080213

Irzon, R., Kurnia, Sendjaja, P., & E. Setiawan, V. (2021). Kaolinitisasi dan mobilitas unsur tanah jarang pada profil pelapukan batuan Gunungapi di Puncak Mandeh, Sumatra Barat. *Buletin Sumber Daya Geologi*, *16*(1), 37–51. https://doi.org/10.47599/bsdg.v16i1.312

Jannat, M. R., Biswas, B., Rahman, M. L., Ahmed, M. F., Hossain, M. J., Khanam, J., & Sharmin, N. (2025). Validity of crystallite size determination methods based on XRD peak broadening in pure and metal-doped nickel ferrites. *Results in Materials*, *28*, 100762. https://doi.org/10.1016/j.rinma.2025.100762

Karlinasari, R., Rahardjo, P. P., & Dajaputra, A. (2023). The Mineral characteristic of tropical residual soil using X-Ray Diffraction (XRD) and Scan Electron Microscopy (SEM). *JACEE (Journal of Advanced Civil and Environmental Engineering)*, *6*(1), 42–56.

Korkanç, M., & Solak, B. (2016). Estimation of engineering properties of selected tuffs by using grain/matrix ratio. *Journal of African Earth Sciences*, *120*, 160–172. https://doi.org/10.1016/j.jafrearsci.2016.05.008

Kudo, T. (2024). Newly identified small vulcanian eruptions during the caldera-forming stage of Towada Volcano, Northeast Japan. *Journal of Volcanology and Geothermal Research*, *452*, 108134. https://doi.org/10.1016/j.jvolgeores.2024.108134

Kusumayudha, S. B., Markam, A. P., & Rahmat, B. (2011). Structure, hydrogeology, and the geothermal system of Mount Ungaran area, Central Java, indonesia. *ICWES 15: The 15th International Conference for Women Engineers and Scientists*, 544–553.

Latif, D. O., Rifa'i, A., & Suryolelono, K. B. (2016). Chemical characteristics of volcanic ash in Indonesia for soil stabilization: Morphology and mineral content. *GEOMATE Journal*, *11*(26), 2606–2610.

Le Bas, Maitre, R. W., Streckeisen, A., & Zanettin, B. (1986). A Chemical Classification of Volcanic Rocks Based on the Total Alkali-Silica Diagram. *Journal of Petrology*, *27*(3), 745–750. https://doi.org/10.1093/petrology/27.3.745

Li, Gaojun, Hartmann, J., Derry, L. A., West, A. J., You, C.-F., Long, X., Zhan, T., Li, L., Li, Gen, Qiu, W., Li, T., Liu, L., Chen, Y., Ji, J., Zhao, L., & Chen, J. (2016). Temperature dependence of basalt weathering. *Earth and Planetary Science Letters*, *443*, 59–69. https://doi.org/10.1016/j.epsl.2016.03.015

Li, X., Han, G., Liu, M., Liu, J., Zhang, Q., & Qu, R. (2022). Potassium and its isotope behaviour during chemical weathering in a tropical catchment affected by evaporite dissolution. *Geochimica et Cosmochimica Acta*, *316*, 105–121. https://doi.org/10.1016/j.gca.2021.10.009

Lin, S.-M., Yu, Y.-L., Zhong, M.-F., Yang, H., Zhang, C.-Y., Zhang, Z.-J., & Wu, Y.-Y. (2023). The dissolution behavior of feldspar minerals in various low-molecularweight organic acids. *Materials*, *16*(20), 6704. https://doi.org/10.3390/ma16206704

Locati, F., Pérez Marfil, P. M., Marfil, S. A., & Lescano, L. (2022). Stability of acid volcanic glasses in alkaline solutions: Understanding their potential to participate in the alkali-silica reaction. *Materials Today Communications*, *31*, 103515. https://doi.org/10.1016/j.mtcomm.2022.103515

Londoño-Restrepo, S. M., Jeronimo-Cruz, R., Millán-Malo, B. M., Rivera-Muñoz, E. M., & Rodriguez-García, M. E. (2019). Effect of the Nano Crystal Size on the X-ray Diffraction Patterns of Biogenic Hydroxyapatite from Human, Bovine, and Porcine Bones. *Scientific Reports*, *9*(1), 5915. https://doi.org/10.1038/s41598-019-42269-9

Meralli, S. (2025). *A Revised Stratigraphic, Tephrochronological and Geochronological Constraint Model of the Depositional Environments of the Sangiran Formation as applied to Hominin Palaeoecological Dynamics*. https://doi.org/10.31235/osf.io/7uwp4_v1

Monasterio-Guillot, L., Rodriguez-Navarro, C., & Ruiz-Agudo, E. (2021). Kinetics and mechanisms of Acid-pH weathering of pyroxenes. *Geochemistry, Geophysics, Geosystems*, *22*(11). https://doi.org/10.1029/2021GC009711

Muslim, R. Q., Kricella, P., Pratamaningsih, M. M., Purwanto, S., Suryani, E., & Ritung, S. (2020). Characteristics of Inceptisols derived from basaltic andesite from several locations in volcanic landform. *SAINS TANAH - Journal of Soil Science and Agroclimatology*, *17*(2), 115. https://doi.org/10.20961/stjssa.v17i2.38221

Nesbitt, H. W., & Young, G. M. (1982). Early Proterozoic climates and plate motions inferred from major element chemistry of lutites. *Nature*, *299*(5885), 715–717. https://doi.org/10.1038/299715a0

Nurcholis, M., Yudiantoro, D. F., Haryanto, D., Dianputra, A. B., & Aji, K. (2019). Process and mineralogy of volcanic materials on the South Side of the Old Lawu Volcano in Java Island. *SAINS TANAH - Journal of Soil Science and Agroclimatology*, *16*(2), 127. https://doi.org/10.20961/stjssa.v16i2.27118

Prentice, M. L., Pittari, A., Barker, S. L. L., & Moon, V. G. (2020). Volcanogenic processes and petrogenesis of the early Pleistocene andesitic-dacitic Maungatautari composite cone, Central Waikato, New Zealand. *New Zealand Journal of Geology and Geophysics*, *63*(2), 210–226. https://doi.org/10.1080/00288306.2019.1656259

Schmid, R. (1981). Descriptive nomenclature and classification of pyroclastic deposits and fragments. *Geologische Rundschau*, *70*(2), 794–799. https://doi.org/10.1007/BF01822152

Schott, J., & Berner, R. A. (1985). Dissolution mechanisms of Pyroxenes and Olivines during weathering. In J. I. Drever (Ed.), *The Chemistry of Weathering* (pp. 35–53). Springer Netherlands. https://doi.org/10.1007/978-94-009-5333-8_3

Shand, S. J. (1927). On the Relations between Silica, Alumina, and the Bases in Eruptive Rocks, considered as a means of classification. *Geological Magazine*, *64*(10), 446–449. https://doi.org/10.1017/S0016756800103760

Sragen Regency Goverment, Pub. L. 11, Peraturan Daerah Kabupaten Sragen No 11 Tahun 2011 Tentang Rencana Tata Ruang Wilayah Kabupaten Sragen Tahun 2011 – 2031 (2011).

Suhendro, I., Al Aro, A. S., Palembang, M. F., Rahim, A. P., & Sari, L. R. (2023). On the formation of lava flows and lava domes in Mafic-Intermediate Magmas (Mount Ungaran, Central Java, Indonesia). *Journal of Volcanology and Seismology*, *17*(3), 228–245. https://doi.org/10.1134/S0742046323700148

Sukardi, & Budhitrisna, T. (1992). *Peta Geologi Lembar Salatiga, Jawa Tengah*. Pusat Penelitian dan Pengembangan Geologi.

Warr, L. N. (2018). A new collection of clay mineral ‘Crystallinity’ Index Standards and revised guidelines for the calibration of Kübler and Árkai indices. *Clay Minerals*, *53*(3), 339–350. https://doi.org/10.1180/clm.2018.42

Zadvernyuk, H., Kadoshnikov, V., Shekhunova, S., & Remez, S. (2021). Particle size distribution and crystallinity as indicators of kaolinite genesis. *Applied Clay Science*, *213*, 106236. https://doi.org/10.1016/j.clay.2021.106236

Zhou, S., Zhou, D., Zhang, Y., & Wang, W. (2019). Study on physical-mechanical properties and microstructure of expansive soil stabilized with fly ash and lime. *Advances in Civil Engineering*, *2019*(1). https://doi.org/10.1155/2019/4693757